Comparative Evaluation and Controller Design of Filter-Based Active Damping for High-Speed PMSM Drives With LC Filter

Ling Meng, Yuan Zhu, and Yunpeng Zhou

***Abstract*—This article compares and evaluates various active damping filter (ADF) techniques and proposes a current controller composed of an all-pass filter (APF) and a dynamic decoupling controller for high-speed permanent magnet synchronous machine equipped with inductor–capacitor filter (LC-HSPMSM). First, a simplified discrete-time domain model of the LC -HSPMSM, incorporating partial separation of high and low frequencies, is developed, which enables the design of the dynamic decoupling controller and facilitates subsequent parameter tuning. Subsequently, a generalized graphical method for evaluating the performance of ADFs is proposed. The robustness against resonance frequency drift and the stability regions of various ADFs are analyzed and compared, with APF determined as the optimal choice based on multiple performance metrics. In addition, a parameter codesign methodology and a comprehensive robustness analysis for the proposed current controller are provided. Finally, the effectiveness and robustness of the proposed method is substantiated through experiments and simulations by operating the 40-kW test motor to 90 kr/min (1500 Hz).**

***Index Terms*—Active damping filter (ADF), inductor–capacitor (LC) filter, high-speed permanent magnet synchronous machine (HSPMSM), multiparameters robustness, single inverter-side current feedback.**

I. Introduction

DUE to the low impedance of the high-speed permanent magnet synchronous motor (HSPMSM), the application of pulsewidth modulation (PWM) will result in a considerable current ripple, which is challenging to mitigate through the implementation of related control algorithms [1], [2]. In addition, the presence of numerous current harmonics gives rise to a notable increase in motor losses, which in turn greatly increases the demand for motor heat dissipation [3]. To reduce the harmonics of the HSPMSM and mitigate the impact of electromagnetic interference, an LC filter can be installed to improve the inverter output voltage quality and consequently lead to an improvement in the motor current quality [4]. This has, in turn, given rise to the necessity for more sophisticated control algorithm designs [5]. In particular, the resonance peak introduced by the LCL circuit has the potential to affect the stability of the current control loop. As stated in [7], different stable regions are given for inverter-side and grid-side current feedback for grid-connected inverter control. It is also highlighted that reasonable design of filter parameters can avoid stability problems. However, for HSPMSM, the operational speed range is broad, and the motor and filter parameters are subject to change, which poses a greater challenge to resonance suppression.

A. Literature Review

A substantial number of research has been dedicated to the development of active damping (AD) strategies, with the objective of effectively addressing the resonance issue. These methods can be categorized into two distinct approaches: open-loop loop shaping methods [9], [10], [11], [12], [13], [14], [15], [16], [17], [18], [19], [20], [21], [22], [23] and closed-loop pole placement methods [24], [25], [26]. The loop shaping methods can be further subdivided into: virtual-resistance damping methods [9], [10], [11], [12], [13], [14], [15], [16] and filter-based damping methods [18], [19], [20], [21], [22], [23], [23]. Due to the fact that full-state feedback control algorithms require more sensors, or the design of complex observers, this type of method is difficult to implement in systems with high switching frequency. Thus, open-loop shaping methods with relatively simple structures are more favored by researchers and industry.

The virtual-resistance method is a widely utilized approach that replaces the actual damping resistor in passive damping technique [8] by introducing an additional feedback loop. Among the different virtual-resistance methods, the effect of the resistance in parallel with the capacitor can be achieved through capacitor–current proportional feedback [10]. However, due to the digital computational delay and zero-order holder (ZOH) effect of PWM, when the LCL resonance crosses the critical frequency (i.e., one-sixth of the sampling frequency) due to parameter changes, the virtual resistance becomes negative and the capacitor–current proportional feedback will fail. To address this issue, a proportional–integral (PI) capacitor–current feedback [11] and a delay compensation link [12] have been introduced to eliminate the adverse effects of the delay and ensure that the AD is equivalent to a positive resistance.

Received 19 June 2025; revised 24 August 2025; accepted 27 September 2025. Date of publication 1 October 2025; date of current version 23 December 2025. This work is funded and supported by the National Key R&D Program of China under Grant 2024YFB4007304. Recommended for publication by Associate Editor F. W. Fuchs. *(Corresponding author: Yuan Zhu.)*

The authors are with the School of Automotive Studies, Tongji University, Shanghai 201800, China (e-mail: 2111311@tongji.edu.cn; yuan.zhu@tongji.edu.cn; 2332890@tongji.edu.cn).

Color versions of one or more figures in this article are available at https://doi.org/10.1109/TPEL.2025.3616306.

Digital Object Identifier 10.1109/TPEL.2025.3616306

The above methods still require capacitor-side current sampling increasing the hardware cost, so virtual resistance in the form of only grid-side current or inverter-side current feedback has been proposed in [13] and [14], respectively. In the context of motor-side current feedback control, a decoupling controller has been proposed in [15] and resonance suppression method in [13] has been adopted. This has demonstrated the feasibility of transplanting the algorithm to the motor control. In [16], a general single-sensor AD framework is proposed to achieve open-loop pole placement with arbitrary damping ratio. This structure can achieve a strong resonance suppression effect, but it requires many parameters to be adjusted and has a complex structure.

In contrast to the virtual-resistance method, the active damping filter (ADF) methods primarily achieves resonance suppression by adjusting the phase-frequency characteristics of the open-loop transfer function [17]. Furthermore, the ADF methods are quite simple compare to the virtual-resistance method, which is favorable for motor control systems operating at high PWM switching and updating frequency. Common filters include notch filter (NF) [18], [19], delay filter (DF) [20], phase-lag filter (PLF) [17], all-pass filter (APF) [21], and low-pass filter (LPF) [22]. Concerning the inverter-side current feedback control, prior work [18] has shown that single NF exhibit suboptimal robustness, necessitating series connections of multiple NFs to ensure adequate phase margin (PM). However, this considerably increases the complexity of the algorithm. To solve the problem of the NF's inability to guarantee the system stability when the resonant frequency crosses one-third of the sampling frequency, a magnitude attenuator is incorporated into the current loop [23], suppressing resonance peaks below 0 dB to stabilize the system. APF has been proposed in [21] to shift the phase of the open-loop system (i.e., -180° phase crossings) into the stable region for AD. However, the article simply analyses the advantages of the APF over the LPF, NF, and PLF, but does not quantify the comparative analyses. At the same time, this article only adjusts the pole parameters of the APF to make the system meet the PM condition at the first cut-off frequency, without considering the PM near the resonant frequency, which may make the high-speed motor system unstable. The dual degree of freedom current control strategy, as outlined in [22], employs LPF to achieve resonance suppression, but is specifically tailored for motor-side current feedback. In addition, due to the presence of the feedforward decoupling controller, the complexity of the algorithm is greatly increased.

For the current loop control algorithm for grid-connected inverters, since its operating frequency is low and basically constant, it is mostly implemented under stationary reference frame (SRF). However, due to the high dynamic response requirements of high-speed motors, current controllers are mostly deployed in the rotating reference frame (RRF) instead of the SRF, resulting in d–q axis cross-coupling issues. In addition, high-speed motors feature a wide operating range, and resonant frequencies shift with speed in the RRF, which poses another challenge for the resonance damping algorithm. Therefore, for LC-HSPMSM drives, the design requirements for the current loop controller are further elevated, and an effective yet simple AD method is essential.

B. Motivation and Innovation

Few studies have addressed the virtual-resistance methods, which relies exclusively on inverter-side current feedback. These methods feature algorithmic complexity [16], tedious parameter tuning [23], and requires consideration of negative resistance condition induced by time delays [14]. According to the literature reviews, compared to the virtual-resistance method, the ADF method has gained greater popularity in motor systems with high PWM switching and update frequencies due to its simpler structure. Despite the proposal of various damping filters, their applications for inverter-side current feedback are limited, with the majority being confined to SRF. Furthermore, there is a paucity of simple and intuitive methods to evaluate existing ADFs and select the optimal filter based on multiple performance indicators.

The majority of studies neglect to consider the motor resistance, focusing exclusively on the LCL component [13], [14], [15], [16], [17], [18], [19], [20], [21]. This approach hinders the subsequent theoretical analysis. [22] undertakes a decomposition of the system model; however, it is only used to design a decoupling controller and is not applied to subsequent parameter design. In addition, in the subsequent parameter selection process, only an approximate range of parameters is given, which is not conducive to the application to motor control systems with different parameters.

Therefore, this article presents three contributions to address these gaps.

1) The system ZOH equivalent model considering the motor resistance is simplified and divided into low- and high-frequency parts in Section II, which not only simplifies the dynamic-decoupling controller design, but also facilitates the subsequent controller parameter design in Section V.
2) For inverter-side current feedback, compared with [18] and [21], a simple and intuitive graphical method for evaluating the robustness of ADFs is proposed in Section III. This method analyzes and compares six common filters: APF, LPF, DF, PLF, NF and quasi-notch filter (QNF) in Section IV, with APF identified as the optimal choice based on multicriteria evaluation.
3) Based on the simplified model, a joint parameter design method of decoupling controller gain and APF pole is proposed in Section V to ensure the PM and gain margin (GM) of the system under the overall frequency domain, thereby achieving the optimal control performance.

In Section VI, not only the robustness of the proposed method is analyzed comprehensively, but also the ADF methods in [18], [19], [21], and [23], as well as the LPF, DF methods are compared. This comparison further demonstrates the superiority of the proposed method. Finally, the effectiveness of the proposed method is verified by experiments and simulations in Section VII on a 40-kW high-speed air compressor for fuel cells up to 90 kr/min (1500 Hz) with a sampling frequency of 40 kHz.

II. System Description and Dynamic-Decoupling Current Controller for LC-HSPMSM Drives

In this section, a simplified LC-HSPMSM model is proposed based on the low-frequency and high-frequency characteristics

TABLE I
PARAMETERS OF THE MOTOR CONTROL SYSTEM

Symbol	Quantity	Value
U_{dc}	DC link voltage	540 V
f_{s}	Sampling and PWM updating frequency	40 kHz
$f_{\max}$	Maximum electrical frequency	1.5 kHz
n_{pp}	Number of pole pairs	1
R_{s}	Stator resistance	0.029 Ω
L_{s}	motor-side inductor	104 μH
C_{f}	inverter-side capacitor	3.3 μF
L_{f}	inverter-side inductor	55 μH
f_{p}	natural resonant frequency	14.61 kHz
ψ_{PM}	Permanent magnet flux linkage	0.026 Wb

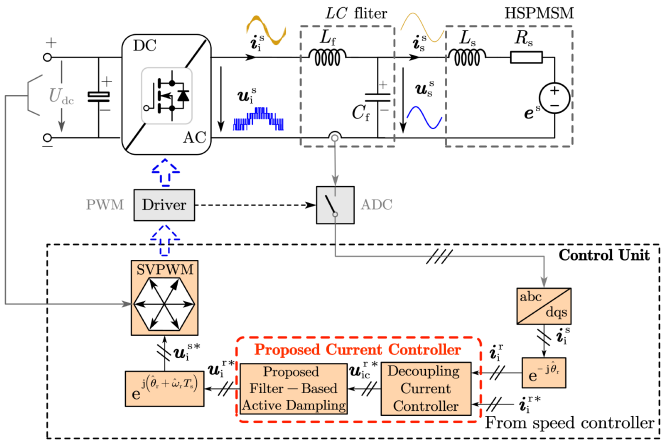

Fig. 1. Complex vector equivalent circuit of the $LC-$HSPMSM in SRF with the proposed current controller. Traditional speed–current cascade control is adopted, and the position θ_{r} and speed ω_{r} information are derived from the sensorless control algorithm. The sampling of signals for FOC is synchronized with the PWM.

of the plant. The effectiveness of the simplified model is validated through comparisons of Bode diagrams with the standard ZOH discretization model. A dynamic-decoupling current loop controller is then designed based on this simplified model to enhance the dynamic tracking performance of the system.

A. Discrete-Time Domain Model for Overall System

Assuming that the three-phase LC filter circuit and the HSPMSM are both *Y*-connected and the three phases are completely symmetrical. Variables in bold italics represent the complex vector, e.g., $\boldsymbol{u}_{\mathrm{s}}^{\mathrm{s}} = u_{\mathrm{d}}^{\mathrm{s}} + \mathrm{j}u_{\mathrm{q}}^{\mathrm{s}}$. The superscript "s" indicates the SRF values, "r" indicates the RRF values, "$*$" for the reference value. The subscript "s" stands for the variables associated with the stator,"i" for the variables associated with the inverter, "d" and "q" for the *d*-axis and *q*-axis values. u stands for voltage, i the current, e the motor back-electromotive force. All parameters of system are provided in Table I, and will be employed in subsequent analyses of the control system and experiments.

The system diagram is depicted in Fig. 1, composed of a three-phase two-level inverter, an LC filter and an HSPMSM. The continuous-time transfer function from the inverter voltage to the inverter current in the SRF can be derived as

$$Y_{\mathrm{ii\_R}}^{\mathrm{s}}(s) = \frac{\boldsymbol{i}_{\mathrm{i}}^{\mathrm{s}}(s)}{\boldsymbol{u}_{\mathrm{i}}^{\mathrm{s}}(s)} = \frac{\frac{1}{L_{\mathrm{f}}}s^2 + \frac{R_{\mathrm{s}}}{L_{\mathrm{s}}L_{\mathrm{f}}}s + \frac{1}{L_{\mathrm{s}}L_{\mathrm{f}}C_{\mathrm{f}}}}{s^3 + \frac{R_{\mathrm{s}}}{L_{\mathrm{s}}}s^2 + \frac{L_{\mathrm{f}}+L_{\mathrm{s}}}{L_{\mathrm{s}}L_{\mathrm{f}}C_{\mathrm{f}}}s + \frac{R_{\mathrm{s}}}{L_{\mathrm{s}}L_{\mathrm{f}}C_{\mathrm{f}}}}. \quad (1)$$

In comparison to the LCL model [7], [16], it is challenging to derive an analytical solution for the discretization of (1), primarily due to the incorporation of motor resistance. Current tracking performance is inherently linked to low-frequency controller design, where the fidelity of the low-frequency model directly impacts controller design precision. This will determines the control system's dynamic response and the controller's decoupling capability [27, Section III-A]. Thus, simplifying the complex model (1) to separate high- and low-frequency parts is essential to streamline controller design.

First, neglecting the effect of resistance in (1), the transfer function of LCL model is considered and can be de decoupled as

$$Y_{\mathrm{ii}}^{\mathrm{s}}(s) = \underbrace{\frac{1}{(L_{\mathrm{f}}+L_{\mathrm{s}})\,s}}_{\text{Low-frequency part}} + \underbrace{\frac{L_{\mathrm{s}}}{L_{\mathrm{f}}\,(L_{\mathrm{f}}+L_{\mathrm{s}})}\frac{s}{s^2+\frac{L_{\mathrm{f}}+L_{\mathrm{s}}}{L_{\mathrm{s}}L_{\mathrm{f}}C_{\mathrm{f}}}}}_{\text{High-frequency part}}. \quad (2)$$

Then, reconsidering the motor resistance and replacing its low-frequency part, transfer function (1) can be simplified to

$$Y_{\mathrm{ii\_R}}^{\mathrm{s}}(s) \approx \underbrace{\frac{1}{(L_{\mathrm{f}}+L_{\mathrm{s}})\,s+R_{\mathrm{s}}}}_{\text{Low-frequency part}} + \underbrace{\frac{L_{\mathrm{s}}}{L_{\mathrm{f}}\,(L_{\mathrm{f}}+L_{\mathrm{s}})}\frac{s}{s^2+\frac{L_{\mathrm{f}}+L_{\mathrm{s}}}{L_{\mathrm{s}}L_{\mathrm{f}}C_{\mathrm{f}}}}}_{\text{High-frequency part}}. \quad (3)$$

By performing the ZOH discretization on (3), the z-domain model in SRF can be derived as

$$\begin{aligned} Y_{\mathrm{ii\_R}}^{\mathrm{s}}(z) &\approx G_{\mathrm{p}}^{\mathrm{s}}(z) = G_{\mathrm{pl}}^{\mathrm{s}}(z) + G_{\mathrm{ph}}^{\mathrm{s}}(z) \\ &= \frac{1-a}{R_{\mathrm{s}}}\frac{1}{z-a} + b\frac{z-1}{z^2-2z\cos(\omega_{\mathrm{p}}T_{\mathrm{s}})+1} \end{aligned} \quad (4)$$

where $G_{\mathrm{pl}}^{\mathrm{s}}(z)$ and $G_{\mathrm{ph}}^{\mathrm{s}}(z)$ are the low-frequency and high-frequency part of transfer function $G_{\mathrm{p}}^{\mathrm{s}}(z)$, respectively. $\omega_{\mathrm{p}} = \sqrt{(L_{\mathrm{f}}+L_{\mathrm{s}})/(L_{\mathrm{s}}L_{\mathrm{f}}C_{\mathrm{f}})}$ is the natural resonant frequency, $b = L_{\mathrm{s}}\sin(\omega_{\mathrm{p}}T_{\mathrm{s}})/[\omega_{\mathrm{p}}L_{\mathrm{f}}(L_{\mathrm{f}}+L_{\mathrm{s}})]$. $a = \mathrm{e}^{-R_{\mathrm{s}}T_{\mathrm{s}}/(L_{\mathrm{s}}+L_{\mathrm{f}})}$.

To verify the effectiveness of this simplification, the Bode plot of (4) and the ZOH equivalent model of (3) obtained from MATLAB `c2d` function are shown in Fig. 2(a). It can be observed that the two are well matched at both high and low frequencies, except for the different amplitude-frequency characteristics at the resonant frequency. Nevertheless, this does not affect the design of the resonance suppression algorithm [7] in high frequency region.

The transfer function (4) in SRF can be transformed into RRF by employing the frequency shift $z \to z\mathrm{e}^{\mathrm{j}\omega_{\mathrm{r}}T_{\mathrm{s}}}$ [16]

$$\begin{aligned} \boldsymbol{G}_{\mathrm{p}}^{\mathrm{r}}(z) &= \boldsymbol{G}_{\mathrm{pl}}^{\mathrm{r}}(z) + \boldsymbol{G}_{\mathrm{ph}}^{\mathrm{r}}(z) \\ &= \frac{1-a}{R_{\mathrm{s}}}\frac{1}{z\mathrm{e}^{\mathrm{j}\omega_{\mathrm{r}}T_{\mathrm{s}}}-a} \\ &\quad + b\frac{z\mathrm{e}^{\mathrm{j}\omega_{\mathrm{r}}T_{\mathrm{s}}}-1}{z^2\mathrm{e}^{2\mathrm{j}\omega_{\mathrm{r}}T_{\mathrm{s}}}-2z\mathrm{e}^{\mathrm{j}\omega_{\mathrm{r}}T_{\mathrm{s}}}\cos(\omega_{\mathrm{p}}T_{\mathrm{s}})+1}. \end{aligned} \quad (5)$$

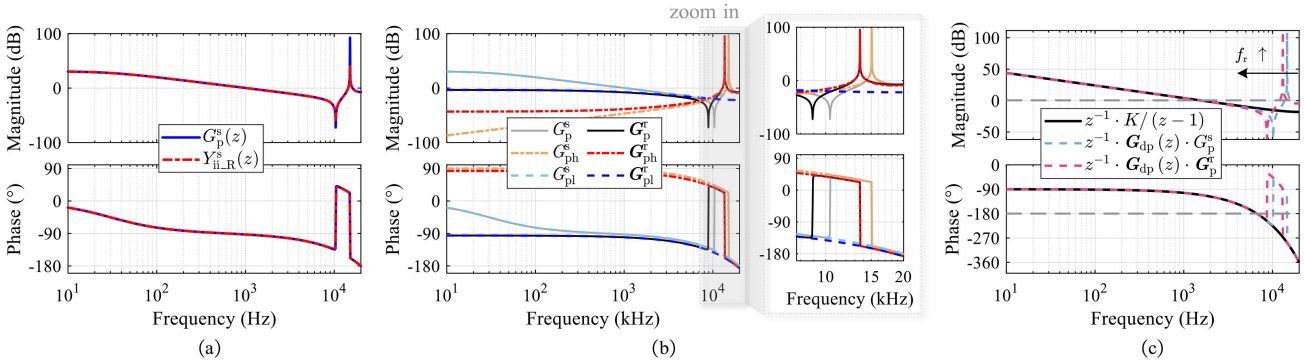

Fig. 2. (a) Bode diagram comparison between $Y^{\mathrm{s}}_{\mathrm{ii\_R}}(z)$ obtained from MATLAB function and its approximation (4). (b) Bode diagram of $G^{\mathrm{s}}_{\mathrm{p}}(z)$, $\boldsymbol{G}^{\mathrm{r}}_{\mathrm{p}}(z)$ under $f_{\mathrm{r}} = 0$, 1500 Hz and their low-frequency and high-frequency parts. (c) Bode diagram of cascade model at different speed ($f_{\mathrm{r}} = 0$, 1500 Hz) and the simplified low-frequency model $z^{-1} \cdot \boldsymbol{G}^{\mathrm{r}}_{\mathrm{pl}}(z)\boldsymbol{G}_{\mathrm{dp}}(z)$, when considering one-step digital delay.

The Bode plot of $G^{\mathrm{s}}_{\mathrm{p}}(z)$ in SRF and $\boldsymbol{G}^{\mathrm{r}}_{\mathrm{p}}(z)$ in RRF are shown in Fig. 2(b). It can be observed that the separated low-frequency and high-frequency components are effective in describing the low-frequency and high-frequency characteristics of $G^{\mathrm{s}}_{\mathrm{p}}(z)$ and $\boldsymbol{G}^{\mathrm{r}}_{\mathrm{p}}(z)$. Moreover, the amplitude contribution of $\boldsymbol{G}^{\mathrm{r}}_{\mathrm{pl}}(z)$ is mainly in the low and middle frequency region, while the amplitude contribution of $\boldsymbol{G}^{\mathrm{r}}_{\mathrm{ph}}(z)$ is concentrated in the resonance frequency region. This indicates that $\boldsymbol{G}^{\mathrm{r}}_{\mathrm{pl}}(z)$ can be employed in the design of the current controller for dynamic current regulation in the low frequency region. Moreover, the frequency-separation property of the simplified model streamlines subsequent control parameter calculation, which will be elaborated upon in Section V.

It is worth noting from Fig. 2(b) that due to the coordinate system transformation, the resonant frequency f_{p} and anti-resonant frequency f_{n} decreases as the speed increases. The synchronous resonant and antiresonant frequency can be expressed as

$$\begin{aligned} f^{\mathrm{r}}_{\mathrm{p}} &= f_{\mathrm{p}} - f_{\mathrm{r}} \\ f^{\mathrm{r}}_{\mathrm{n}} &= f_{\mathrm{n}} - f_{\mathrm{r}}. \end{aligned} \tag{6}$$

Unlike grid-connected converter, due to the wide operating range of HSPMSM, the synchronous resonant frequency will exhibit a significant degree of variation over a broad range, which will in turn affect the stability of the system.

B. Dynamic-Decoupling Current Controller

As illustrated in Fig. 2(b), we can also see that when the rotational speed is not zero, the amplitude–frequency characteristics of $\boldsymbol{G}^{\mathrm{r}}_{\mathrm{pl}}(z)$ is gradually shifted downward, accompanied by cross-coupling between the dq-axes in the current dynamics [27]. To enhance the dynamic performance, it is recommended that a dynamic-decoupling current controller based on the pole-zero cancellation method [27] should be employed. This can be expressed as follows:

$$\begin{aligned} \boldsymbol{G}_{\mathrm{dp}}(z) &= \left(\boldsymbol{G}^{r}_{\mathrm{pl}}(z)\right)^{-1} \cdot \frac{K}{z-1} \\ &= K\frac{R_{\mathrm{s}}}{1-a}\frac{z\mathrm{e}^{\mathrm{j}\omega_{\mathrm{r}}T_{\mathrm{s}}} - a}{z-1} \end{aligned} \tag{7}$$

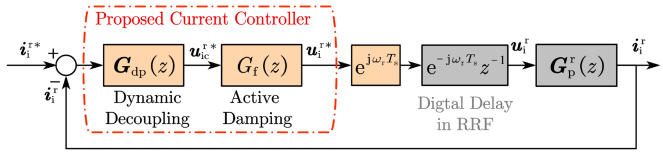

Fig. 3. Block diagram of the inverter-side current control loop.

where K is the gain of the dynamic-decoupling current controller.

III. Stability Analysis of LC-HSPMSM Drives

In this section, the stability of the LC-HSPMSM system will be examined with and without the introduction of ADF, comprising two key parts:

1) First, stability conditions for the undamped system (without ADF) are first derived. Analysis demonstrates that these conditions cannot be satisfied for the motor control system studied in this article, necessitating the incorporation of ADF to ensure stability.
2) A general graphical method is proposed to evaluate the robustness and effectiveness of different ADFs, and will be employed in Section IV to identify the optimal ADF design.

A. Stability Analysis of Inverter-Side Current Feedback Control Without ADF

The system block diagram illustrated in Fig. 1 can be simplified to the closed-loop control system shown in Fig. 3. The current controller containing decoupling controller and ADF, computational delay and ZOH equivalent model (5) are depicted in this figure.

The open-loop transfer function in z-domain can be derived as

$$\boldsymbol{G}_{\mathrm{ol}}(z) = z^{-1}\boldsymbol{G}_{\mathrm{dp}}(z)G_{\mathrm{f}}(z)\boldsymbol{G}^{\mathrm{r}}_{\mathrm{p}}(z). \tag{8}$$

According to (8), the phase of open-loop transfer function can be defined as

$$\vartheta_{\mathrm{t}} = \vartheta_{\mathrm{dp}} + \vartheta_{\mathrm{f}} + \vartheta_{\mathrm{d}} + \vartheta_{\mathrm{p}} \tag{9}$$

where ϑ_{dp}, ϑ_{f}, ϑ_{d}, and ϑ_{p} are the phase of $\boldsymbol{G}_{\mathrm{dp}}(z)$, $G_{\mathrm{f}}(z)$, z^{-1} and $\boldsymbol{G}_{\mathrm{p}}^{\mathrm{r}}(z)$, respectively. Among them, the phase ϑ_{d} of z^{-1} can be simply expressed as

$$\vartheta_{\mathrm{d}} = \angle \mathrm{e}^{-\mathrm{j}2\pi f T_{\mathrm{s}}} = -2\pi f T_{\mathrm{s}}. \tag{10}$$

As illustrated in Fig. 2(c), due to the decoupling controller, the phase of $\boldsymbol{G}_{\mathrm{dp}}(z)\cdot\boldsymbol{G}_{\mathrm{p}}^{\mathrm{r}}$ can be reduced to the phase of $K/(z-1)$ except the resonant frequency region, e.g., $\vartheta_{\mathrm{p}}+\vartheta_{\mathrm{dp}} \approx \angle(1/(\mathrm{e}^{-\mathrm{j}2\pi(f)T_{\mathrm{s}}}-1))$ [7]

Substituting all these simplifications into ϑ_{t} gives

$$\vartheta_{\mathrm{t}}(f) = \begin{cases} \vartheta_{\mathrm{f}} - 3\pi f T_{\mathrm{s}} - \pi/2 & (f < f_{\mathrm{n}}^{\mathrm{r}}) \\ \vartheta_{\mathrm{f}} - 3\pi f T_{\mathrm{s}} + \pi/2 & (f_{\mathrm{n}}^{\mathrm{r}} < f < f_{\mathrm{p}}^{\mathrm{r}}) \\ \vartheta_{\mathrm{f}} - 3\pi f T_{\mathrm{s}} - \pi/2 & (f > f_{\mathrm{p}}^{\mathrm{r}}) \end{cases}. \tag{11}$$

According to the definition of Nyquist stability criterion, in order to stabilize this control system, the phase-frequency characteristics of the system must avoid traversing $-\pi+2k\pi$ (where k is an integer) at the resonant frequency [7], [19], which can be expressed as follows:

$$\begin{cases} \theta_{\mathrm{f}} - 3\pi f_{\mathrm{p}}^{\mathrm{r}} T_{\mathrm{s}} + \pi/2 < -\pi + 2k\pi \\ \vartheta_{\mathrm{f}} - 3\pi f_{\mathrm{p}}^{\mathrm{r}} T_{\mathrm{s}} - \pi/2 > -3\pi + 2k\pi. \end{cases} \tag{12}$$

In practice, excessive phase lag should be avoided. Therefore, it is sufficient to consider the cases of $k=0$ and 1. For the open-loop system (8) without ADF ($G_{\mathrm{f}}(z)=1$), the range of $f_{\mathrm{p}}^{\mathrm{r}}$ that enables stabilization can be derived as

$$\begin{cases} f_{\mathrm{s}}/2 < f_{\mathrm{p}}^{\mathrm{r}} < 5f_{\mathrm{s}}/6, & k=0 \\ 0 < f_{\mathrm{p}}^{\mathrm{r}} < f_{\mathrm{s}}/6, & k=1. \end{cases} \tag{13}$$

1) When $k=0$. In order to effectively suppress the current ripple, the natural resonant frequency of the LC filter is generally designed to be less than $f_{\mathrm{s}}/2$ [5], which implies that $f_{\mathrm{p}}^{\mathrm{r}} = f_{\mathrm{p}} - f_{\mathrm{r}} < f_{\mathrm{s}}/2 - f_{\mathrm{r}}$. Due to the constraint inherent to the LC filter design, this scenario does not hold.

2) When $k=1$. For most of the motor systems, inductors and capacitors of LC filter with relatively low inductance and capacitance values are typically employed to reduce costs [6]. For the system studied in this paper, the natural resonance frequency is 14.61 kHz, which is greater than $f_{\mathrm{s}}/6$. Consequently, this resonance frequency also falls outside the stable range.

It can be concluded that, in the context of the LC-HSPMSM control system under examination in this paper, inverter-side current feedback control without AD can lead to instability. Therefore, it is necessary to introduce the ADF to reshape the open-loop phase frequency characteristics and thereby stabilize the system.

B. Stability Analysis of Inverter-Side Current Feedback Control With the Addition of ADF

The ADF introduces additional phase to the open-loop system $\boldsymbol{G}_{\mathrm{ol}}(z)$, allowing it to satisfy the PM criteria and guaranteeing stability. By solving the aforementioned inequality (12), it is possible to ascertain the phase range that the additional filter should provide at varying $f_{\mathrm{p}}^{\mathrm{r}}$

$$\begin{aligned} 3\pi f_{\mathrm{p}}^{\mathrm{r}} T_{\mathrm{s}} - 5\pi/2 + 2k\pi < \vartheta_{\mathrm{f}}\left(f_{\mathrm{p}}^{\mathrm{r}}\right) \\ < 3\pi f_{\mathrm{p}}^{\mathrm{r}} T_{\mathrm{s}} - 3\pi/2 + 2k\pi. \end{aligned} \tag{14}$$

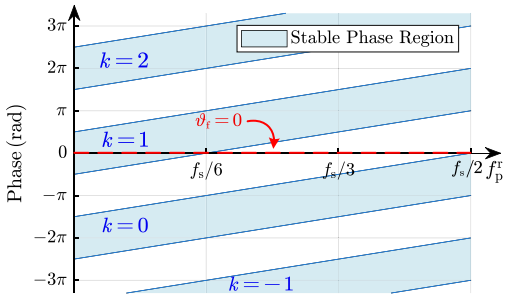

Fig. 4. Stable phase region of ADF with $k=-1, 0, 1, 2$.

It can be demonstrated that, under a specific $f_{\mathrm{p}}^{\mathrm{r}}$, if $\vartheta_{\mathrm{f}}(f_{\mathrm{p}}^{\mathrm{r}})$ remains within the solution region of (14), then no stability issues will arise. In other words, the aforementioned (14) delineates a set of linear programming regions, and the solution to these inequalities represent the phase range that the ADF should provide at different resonant frequencies $f_{\mathrm{p}}^{\mathrm{r}}$ to maintain system stability. Thus, the boundaries of inequalities are plotted in Fig. 4, and the stable phase regions are denoted by the blue shaded area. Although the resonant frequency $f_{\mathrm{p}}^{\mathrm{r}}$ will shift with the change of speed and parameters, it remains within range $(0,\ f_{\mathrm{s}}/2)$.

Still take the example of the motor using inverter-side current feedback control without ADF. In this instance, $\vartheta_{\mathrm{f}}=0$, as illustrated by the red straight line in Fig. 4, intersects with the boundary of the stable phase region at points $f_{\mathrm{s}}/6$ and $f_{\mathrm{s}}/2$, indicating stability only when $0 < f_{\mathrm{p}}^{\mathrm{r}} < f_{\mathrm{s}}/6$. Outside the stable phase region, system stability cannot be guaranteed. These conclusions are the same as the calculation and analysis results in (13).

The ADF stable phase region is an effective tool to evaluate the stability and robustness of the LC-HSPMSM control system based on ADF under resonant frequency drift, offering a straightforward approach for practical implementation.

IV. Evaluation of Existing Damping Filters

Based on the preceding ADF stability analysis, this section conducts qualitative and quantitative evaluations of different damping filters to assess their performance and identify the most suitable option.

Commonly used damping filters—LPF, APF, DF, PLF, NF, and QNF—are analyzed. Their transfer functions in the s-domain are listed in Table II. For practical implementation, the filters need to be transformed into z-domain. The generalized equation after discretization (20) and their detailed parameters are given in Appendix A. The phase-frequency characteristics of the z-domain filter are plotted inside the Fig. 4, thus generating Fig. 5(a) and (b), which serve as a metric to evaluate the filter robustness to resonance frequency shift.

A. First-Order Filters

After introducing the different first-order filters, the ADF stability regions of the system are illustrated in Fig. 5(a). From this phase diagram, it can be observed that APF, DF, and LPF are all capable of achieving a continuous and large range of

TABLE II
EXISTING FILTERS FOR AD

Filter	Transfer function	Parameters
Low-Pass Filter (LPF)	$\frac{\omega_c}{s+\omega_c}$	ω_c: cut-off frequency
All-Pass Filter (APF)	$\frac{\omega_a - s}{s+\omega_a}$	ω_a : $-90°$ phase frequency
Delay Filter (DF)	e^{-sT_s}	/
Phase Lag Filter (PLF)	$\frac{\omega_{pf}}{\omega_{zf}} \cdot \frac{s+\omega_{zf}}{s+\omega_{pf}}$	ω_{pf}: pole corner frequency ω_{zf}: zero corner frequency
Notch Filter (NF)	$\frac{s^2+\omega_n^2}{s^2+2\zeta_n\omega_n s+\omega_n^2}$	ω_n: notch frequency ζ_n: damping ratio
Quasi-Notch Filter (QNF)	$\frac{s^2+2\zeta_p\omega_n s+\omega_n^2}{s^2+2\zeta_z\omega_n s+\omega_n^2}$	ω_n: notch frequency ζ_p: damping ratio of ploe ζ_z: damping ratio of zero

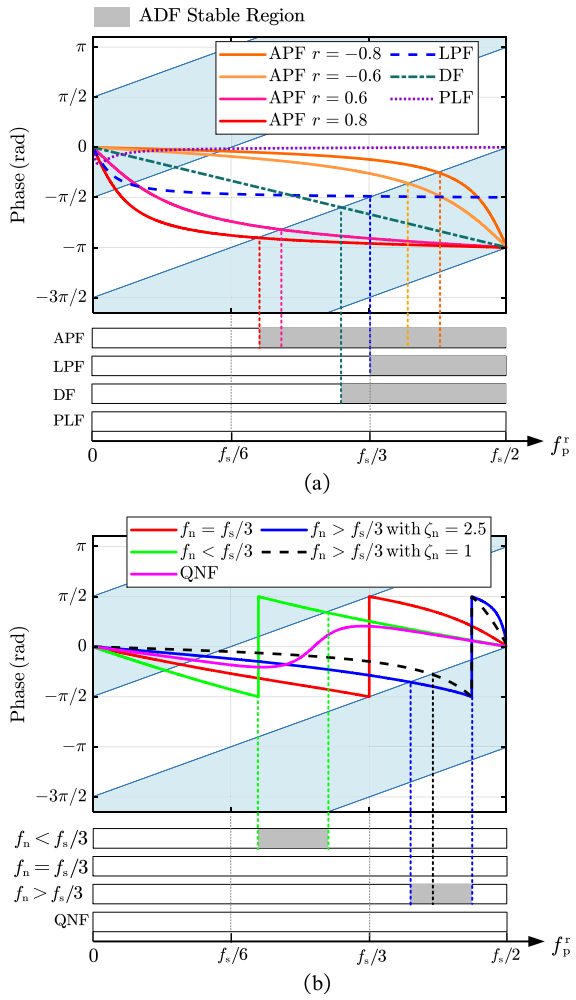

Fig. 5. ADF stability regions of the different filters, denoted by gray areas. As analyzed in Section III-A, it is only necessary to focuses on the ADF stable region in $(f_s/6, f_s/2)$. (a) First-order filters. (b) NF and its quasi-form.

stable frequency ranges. Moreover, APF offers the largest range of ADF stability regions among the first-order filters under consideration. In contrast, PLF exhibits the minimum APF stable region which is mainly concentrated in interval $(0, f_s/6)$. This area is not considered in the system described in this article.

The transfer function of APF after discretization is

$$G_{apf} = \frac{-rz+1}{z-1} \tag{15}$$

where r is the pole of the APF. It was claimed that APF are not suitable for inverter-current feedback control if the resonant frequency f_p^r is located between $f_s/6$ and $f_s/3$ [21, Section IV]. However, as can be seen from Fig. 5(a), when r approaches 1, the stable frequency range of APF is the largest with a limit of $(f_s/6, f_s/2)$. As there is no parameters in DF, its stable frequency range remains constant, which is $(3f_s/10, f_s/2)$. The LPF has a stable frequency range with a limit of $(f_s/3, f_s/2)$. The stable frequency region of the APF is the broadest among these first-order filters, indicating that the APF exhibits superior tolerance to resonant frequency drift.

Moreover, in contrast to LPF, APF does not alter the amplitude–frequency characteristics of the system. In comparison to DF, even for multiples of the delay [20], APF demonstrates enhanced flexibility in phase alternation, exhibiting a larger ADF stable region. In terms of digital realization, APF has a single adjustable parameter, a straightforward structure, and easy to implement. It can thus be concluded that APF has obvious advantages in the AD application of filters.

B. NF and its Quasi-Form

The frequency responses of NFs with different notch frequency and damping ratio, along with their quasi-form (QNF) are depicted in Fig. 5(b). The NF intuitively performs the task of zero-pole cancellation to achieve resonance suppression. However, this becomes challenging due to potential shifts in the resonance frequency from various factors. Instead, NF is more commonly used to produce a phase lag or lead in proximity to the resonance frequency, thereby stabilizing the system [18].

For inverter-side current feedback control, the ADF stable region with NF has been identified in [18], but the analysis was quite complex and difficult to implement. This entails considering not only which frequency band the resonant frequency is located in, but also its magnitude with respect to the notch frequency [18, Section III-B]. The utilization of the graphical approach proposed herein facilitates the stability analysis and intuitive design of the notch frequency of the NF. Specifically, when $f_n = f_s/3$, the NF is incapable of stabilising the system, on account of the fact that it does not intersect the upper and lower stable region; when $f_n > f_s/3$, the NF should provide a phase lead to stabilize the system; and when $f_n < f_s/3$, a phase lag should be provided. In terms of the QNF, due to the addition damping in the numerator of the NF, it cannot provide sufficient lead or lag phase at notch frequency, making it less robust, with a minimum ADF stable range. As can be seen from Fig. 5(a) and (b), the ADF sable region is quite narrow and less expansive than that of first-order filters. Therefore, NF and QNF are less

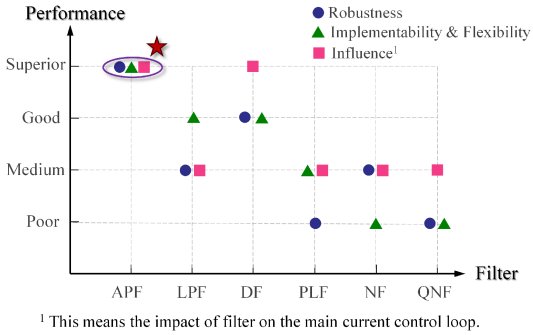

Fig. 6. Performance comparison among different filters. The optimal candidate filter is represented by a star scatter symbol.

robust and are not recommended for the inverter-side current feedback control.

C. Discussion

Different from the conventional method of judging the phase-frequency characteristics of the system open-loop transfer function [18], [19], [21], [22], [23], our contribution lies in its innovative and intuitive graphical method that enables direct comparison of multiple ADFs and offers intuitive stability insights. In addition, when filter parameters vary, the method allows direct visualization of how parameter changes affect the stable region. The effectiveness and robustness of the graphical method will be validated through the experiments and simulations in Section VII.

According to the above analysis, the performance of different filters are summarized in Fig. 6. The first-order filters except PLF offer a continuous ADF stable region, and are suitable for practical use due to their high robustness and simple implementation. Comparative analysis also revels that the best performance can be achieved by applying APF for inverter-side current feedback control.

V. Parameters Co-Design of the Proposed Current Controller

The preceding comparative analysis identifies that APF is the optimal solution for inverter-side current feedback control. Thus, the proposed current controllers is designed using APF combined with dynamic decoupling controller, where the pole r of the $G_{\text{apf}}(z)$ and the gain K of $\boldsymbol{G}_{\text{dp}}(z)$ are co-designed to satisfy the system's PM and GM requirements in both the low- and high-frequency region.

A. Effect of Parameters r and K on System Stability

Based on the simplified model (5) and control loop in Fig. 3, the low- and high-frequency open-loop transfer functions $\boldsymbol{G}_{\text{oll}}(z)$ and $\boldsymbol{G}_{\text{olh}}(z)$ are derived in (16), and their frequency responses are depicted in Fig. 7(a)

$$\boldsymbol{G}_{\text{ol}}(z) = \underbrace{z^{-1}\boldsymbol{G}_{\text{dp}}(z)G_{\text{f}}(z)\boldsymbol{G}_{\text{pl}}^{\text{r}}(z)}_{\boldsymbol{G}_{\text{oll}}(z)} + \underbrace{z^{-1}\boldsymbol{G}_{\text{dp}}(z)G_{\text{f}}(z)\boldsymbol{G}_{\text{ph}}^{\text{r}}(z)}_{\boldsymbol{G}_{\text{olh}}(z)}. \tag{16}$$

Since the plant (5) is separated into low- and high-frequency parts, the cut-off frequency f_{cp1} of the system at low frequencies can be calculated simply from $\boldsymbol{G}_{\text{oll}}(z)$, while the cut-off frequency f_{cp2} near the resonance from the high-frequency part $\boldsymbol{G}_{\text{olh}}(z)$, as can be seen from Fig. 7(a). The detailed derivation of cut-off frequencies can be found in the Appendix B. Due to the implementation of the decoupling controller, the f_{cp1} at low frequencies does not vary with rotational speed as a function of K only. Whereas f_{cp2} at high frequencies changes at different rotational speeds because of the resonance frequency drift. Once cut-off frequencies are established, the PM of the system can be calculated and designed in accordance with the criteria.

The parameter K is instrumental in determining the bandwidth of the closed-loop system and directly influences the PM. An increase in K results in a decrease in PM1. In addition, it will also lead to an augmentation in the amplitude at the resonance frequency, expanding the frequency range above the 0 dB line and concomitantly reducing the stability margin PM2. It is also worth noting that the pole r of APF, as seen in Fig. 5(a), again affects the stability margin of the system. Increasing r results in an improvement to the PM2 in the vicinity of the resonance, but leads to a decrease in the PM1 at low frequency. Thus, r and K should be jointly designed to achieve optimal control performance over the full frequency range.

B. Proposed Parameters Co-Design for APF-Based AD

From the phase diagram of APF in Fig. 5(a), increasing the pole r of the APF leads to greater phase lag. Consequently, the value of pole r can be calibrated to guarantee the requisite phase lag at a designated frequency. The phase of APF can be derived from (15) as follows:

$$\vartheta_{\text{apf}}(f) = -2\pi f T_{\text{s}} - 2\arctan\left[\frac{r\sin(2\pi f T_{\text{s}})}{1 - r\cos(2\pi f T_{\text{s}})}\right]. \tag{17}$$

If a phase lag, ϑ_{cp}, is specified at the desired frequency f_{cp}, then the pole r can be solved as

$$r = \frac{c}{c\cdot\cos(2\pi f_{\text{cp}}T_{\text{s}}) - \sin(2\pi f_{\text{cp}}T_{\text{s}})} \tag{18}$$

where $c = \tan[(\vartheta_{\text{cp}} + 2\pi f_{\text{cp}}T_{\text{s}})/2]$.

As previously analyzed, it is necessary to systematically consider the parameter design of r and K in an integrated manner, with a focus on the system stability margin indexes. Typically, to ensure the robustness of the system, the stability margin, i.e., PM$> \pi/4$ and GM> 3 dB, should be satisfied [16].

The PM in two cut-off frequencies can be expressed as

$$\begin{cases} \vartheta_{\text{apf}}(f_{\text{cp1}}) - 3\pi f_{\text{cp1}}T_{\text{s}} - \frac{\pi}{2} \geq -\pi + \text{PM1} \\ \vartheta_{\text{apf}}(f_{\text{cp2}}) - 3\pi f_{\text{cp2}}T_{\text{s}} + \frac{\pi}{2} \leq -\pi - \text{PM2} \end{cases}. \tag{19}$$

Thus, when PM1 $=$ PM2 $= \pi/3$, the angle $\vartheta_{\text{apf}}(f_{\text{cp}})$ can be calculated at different f_{cp1} and f_{cp2} as the boundary of the stable region. Since both $\vartheta_{\text{apf}}(f_{\text{cp}})$ and f_{cp} are known, the parameter r can be calculated from (18). Ultimately, by combining (18),

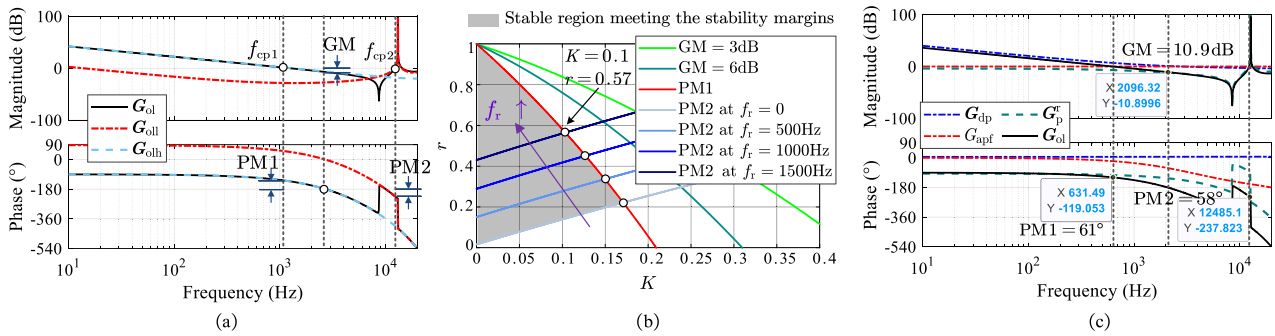

Fig. 7. (a) Bode diagram of $\boldsymbol{G}_{\rm olh}(z)$, $\boldsymbol{G}_{\rm oll}(z)$, and $\boldsymbol{G}_{\rm ol}(z)$ under $f_{\rm r} = 1500$ Hz with all stability margins (PM1, GM and PM2) marked. (b) Parametric design plane of $K - r$ defined by the stability boundary curves, i.e., GM $= 3$ dB, PM1 $= \pi/3$ and PM2 $= \pi/3$ under different $f_{\rm r}$. (c) Bode diagram of $\boldsymbol{G}_{\rm ol}(z)$ under $f_{\rm r}$ $= 1500$ Hz with precalculated controller parameters from (b).

(19), (24), and (26), the relationship between r and K under the PM constraints can be derived. The K-r boundary lines and stable region are depicted in Fig. 7(b). As can be observed, the boundary of PM2 will move upwards as speed increase, thereby shrinking the stable region. This highlights the critical need for stability design in LC-HSPMSM system. In addition, the intersection of high- and low-frequency stability boundaries defines the maximum achievable K and corresponding r at a given speed, satisfying the system's stability margin requirements while ensuring adequate dynamic performance.

The present study has focused exclusively on the calculation of the stable region of the system on the basis of PM, but has not taken GM into consideration. It is possible to obtain $-\pi$ crossover frequency based on (11) and (17). Subsequently, GM can be calculated based on the magnitude–frequency characteristics of $G_{\rm oll}(z)$ at the crossover frequency. It can also be expressed as a functional form of K-r. The graphical representation of this function is depicted in Fig. 7(b), elucidating that the GM boundary is substantially larger than the PM boundaries. Consequently, the GM boundary can be disregarded during the design process of parameters.

Taking the operating frequency of 1500 Hz as an example, the APF parameters r and decoupling controller parameters K are designed, where the system parameters are shown in Table I. The parameters design can be divided into two following steps.

1) First, two cut-off frequencies are calculated according to (24) and (26), and then the stable boundaries of high frequency and low frequency are calculated according to (18) and (19).
2) The intersection of the PM1 and PM2 boundaries is used as the designed parameter value, in order to ensure the stability and dynamic performance of the system. As can be seen in (18) and (19), the specific value of the intersection can be obtained by making the two boundaries equal.

In the case of $f_{\rm r} = 1500$ Hz, $r = 0.57$ and $K = 0.1$ are obtained, as shown in Fig. 7(b). The Bode diagram of the open-loop transfer function of the final designed system is illustrated in Fig. 7(c). It can be seen that even though the cut-off frequency is simplified in the calculation, the PM obtained is more accurate and only differs from the desired value by $1 \sim 2^\circ$. Furthermore, the GM also meets the system stability requirements, which is consistent with the previous analysis. In other rotation frequencies, K and r can also be designed according to the above steps.

It can thus be concluded that, through the collaborative design of r and K as follows:

1) The stability index of the system at high and low frequencies can be satisfied as much as possible.
2) The system response will not slow down by excessively lowering K due to system stability requirements.

VI. Robustness Analysis

A. Robustness Against Parameter Errors

Generally, the motor resistance $R_{\rm s}$ and the motor inductance $L_{\rm s}$ exhibit a variation of $\pm 50\%$. Since the selected filter inductance value is small with a soft magnetic alloy powder core, the parameter deviation caused by manufacturing error and magnetic saturation will not exceed $\pm 15\%$ [6]. Furthermore, the majority of the filter capacitors adopt thin film capacitors. The manufacturing error and the change with current and temperature are also small, about $\pm 10\%$ totally.

The pole maps of the close-loop system with mismatched parameters for the methods in [18], [19], [21], [23], LPF, DF and proposed method are compared in Fig. 8 at $f_{\rm r} = 1500$ Hz. Evidently, the parameter selection method proposed in this article incorporates full-frequency-domain stability indices, ensuring parameter robustness across a wider range of parameter variations compared to the approach in [21]. In the HSPMSM system studied herein, the resonant frequency $f_{\rm p}^{\rm r}$ has reached 13.11 kHz at $f_{\rm r} = 1500$ Hz, which is lower than $f_{\rm s}/3$. Both LPF and NF methods fail to guarantee system stability, which is consistent with the results in Fig. 5. Although the DF method can guarantee stability at 1500 Hz, its parameter robustness is much less than that of the APF method. It is worth noting that although the method in [23] exhibits comparable robustness to the proposed approach, its pole damping ratio is relatively low. This is expected to result in larger current fluctuations and higher THD than those achieved by the proposed method, which will be verified in the experiment in Section VII-C.

Furthermore, two phenomena are worth noting from the pole maps of proposed method as follows:

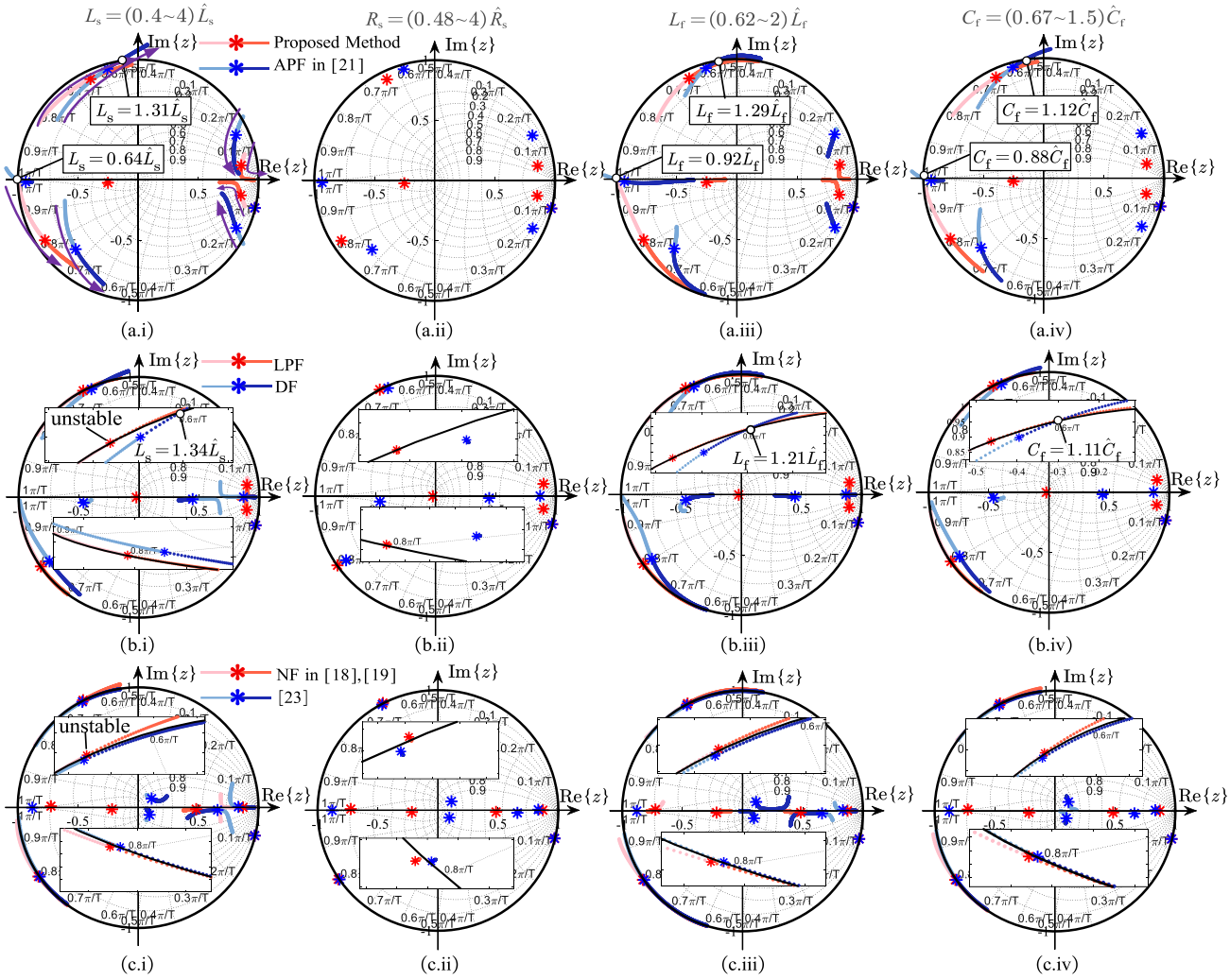

Fig. 8. Comparison of root-locus when the parameter (L_s, L_f, C_f, R_s) varies from small to large at $f_r = 1500$ Hz. Nominal values are indicated by $*$ symbol. The arrows indicate the direction in which the parameter is increasing, with the color scale ranging from light to dark. The proposed method maintains stability across the entire parameter variation range. (a.i)-(a.iv) for proposed method and APF in [21]. (b.i)-(b.iv) for LPF and DF. (c.i)-(c.iv) for NF in [18], [19] and improved NF in [23].

1) The control system is more sensitive to capacitance parameters and can tolerate the smallest range of parameter variations. However, since the capacitors themselves are less variable in practice, the range of parameter variation under system stabilization still meets the desired requirements.
2) The APF method is more robust to the parameter mismatch situation caused by parameter increase.

The underlying reason for these phenomenons can be elucidated by the fact that when the parameters are varied in the same proportion, the resonance frequency shift caused by a decrease in the parameters is much larger than in the case of an increase in the parameters, as shown in Fig. 9. In addition, the resonant frequency shift for a given percentage change in C_f is greater than that caused by the corresponding change in L_s and L_f.

In order to further verify the robustness of the proposed algorithm, stability analysis under multiparameter mismatch is performed. From the previous analysis, it can be seen that the effect of R_s on the robustness of the system parameters is small, so it is only necessary to analyze the case of mismatch of the parameters L_s, C_f, and L_f. The root locus under the variation of the L_s, when the filter parameter varies by $\pm 15\%$ are depicted

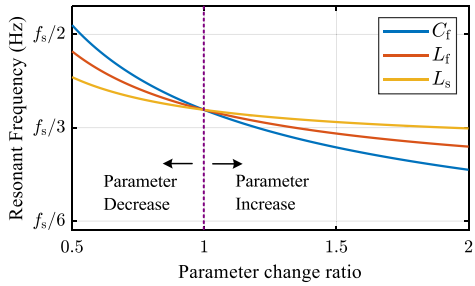

Fig. 9. Resonant frequency shift caused by different parameters variation.

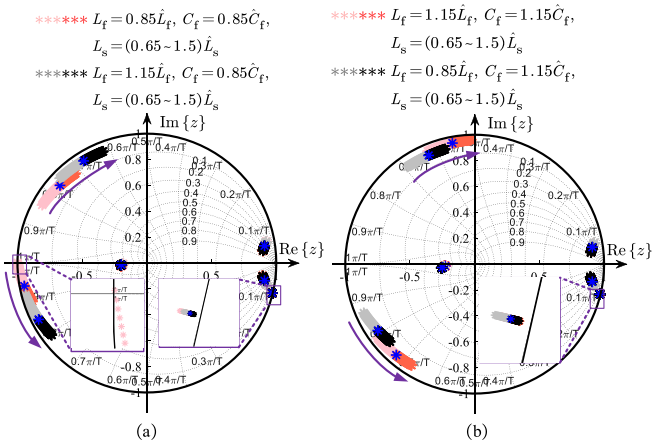

Fig. 10. Loci of the closed-loop poles when L_s varies under filter parameter mismatch, at $f_r = 1500$ Hz. (a)$L_f = 0.85\hat{L}_f, C_f = 0.85\hat{C}_f$ and $L_f = 1.15\hat{L}_f, C_f = 0.85\hat{C}_f$. (b)$L_f = 1.15\hat{L}_f, C_f = 1.15\hat{C}_f$ and $L_f = 0.85\hat{L}_f, C_f = 1.15\hat{C}_f$.

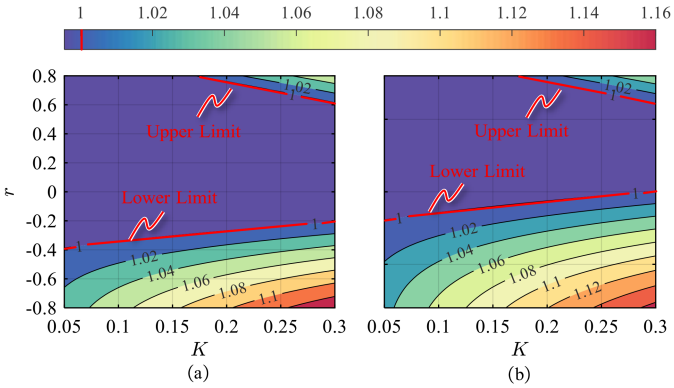

Fig. 11. The maximum amplitude value of poles with different controller parameters. (a)$f_r = 500$ Hz. (b)$f_r = 1500$ Hz.

in Fig. 10. The results illustrate that even in the case of filter parameters mismatch, the system can still tolerate a variation of L_s 0.65 times to 1.5 times.

B. Robustness Against Controller Parameters

When the controller parameters are varied, maximum amplitude value of poles at different speeds are shown in Fig. 11. When the gain K is small, the low-frequency stability margin is high. The second cut-off frequency f_{cp2} increases inversely with K, allowing the APF to stabilize the system by providing phase lag at f_{cp2} with a small r. Even when r is large, leading to substantial phase lag, the phase response at the second cut-off frequency remains unlikely to cross $-180^\circ + 2k\pi$, as evidenced by transfer function $\boldsymbol{G}_p^r(z)$ and $\boldsymbol{G}_{ol}^r(z)$ in Fig. 7(c). Conversely, as K increases, the low-frequency stability margin diminishes, necessitating a reduction in the maximum allowable value of r to prevent excessive phase lag at the first cut-off frequency f_{cp1}. At the same time, since f_{cp2} decreases as K increases, the phase lag provided by the APF at f_{cp2} should increase, so the corresponding lower limit of r will rise. This interdependence

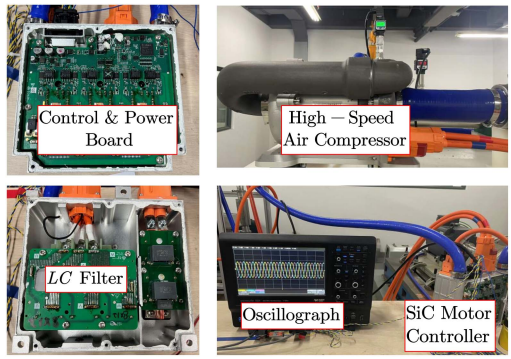

Fig. 12. Experimental platform of LC-HSPMSM.

underscores the necessity of jointly optimizing parameters r and K.

VII. Simulation and Experimental Results

Simulations and experiments are undertaken on a 40-kW high-speed air compressor for fuel cells to assess the effectiveness and feasibility of the proposed current controller. The test bench is depicted in Fig. 12 and the Infineon AURIX TC387 is utilized to implement control algorithms with switching and sampling frequency up to 40 kHz. The system parameters used in the simulation and experiment are consistent with the above theoretical analysis as shown in Table I.

A. Simulation Comparison With Different Filter-Based Damping

In order to demonstrate the superiority of the APF method and verify the accuracy and effectiveness of the graphical method in Section IV, Fig. 13 gives the comparison results of different filter-based AD method.

For LPF-based method, considering the PM in both low-frequency and high-frequency regions, the LPF cut-off frequency is set to 15000 rd/s, and the decoupling controller parameters are consistent with the APF method. According to Fig. 5(a), the stable region of the LPF is $(f_s/3, f_s/2)$. It is calculated that when the speed exceeds 76.4 kr/min, the resonant frequency will be lower than the boundary of the stable region and the system will become unstable. As demonstrated in Fig. 13(b), the instability speed 74.0 kr/min is found to be in close proximity to the calculated result.

Given that the unstable speed of DF in Fig. 5(a) was calculated as 156.4 kr/min, exceed the maximum system speed 90 kr/min under the specified parameters, a robustness comparison was made between the DF and APF method. When the inductance parameter of the LC filter is changed to 1.4 times the nominal parameter, the resonant frequency of the system is changed to 13.2 kHz, and the unstable speed of the DF is 70.3 kr/min. The instability speed in Fig. 13(b) is 73.2 kr/min, which is also close to the calculated value.

To further demonstrate the excellent performance of APF, after the motor reaches 90 kr/min, the LC filter inductance is increased to twice the nominal value, as illustrated in Fig. 13(a).

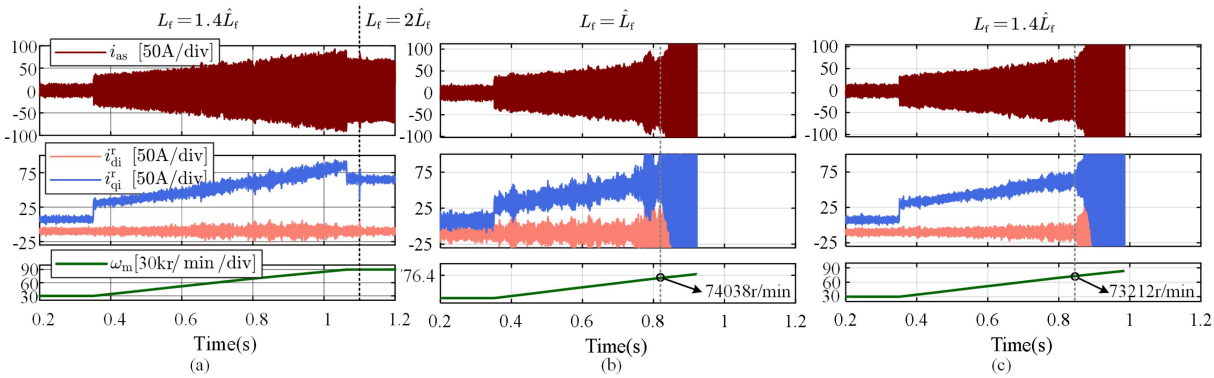

Fig. 13. Simulation results of different filter-based AD method. (a) APF-based AD. (b) LPF-based AD. (c) DF-based AD.

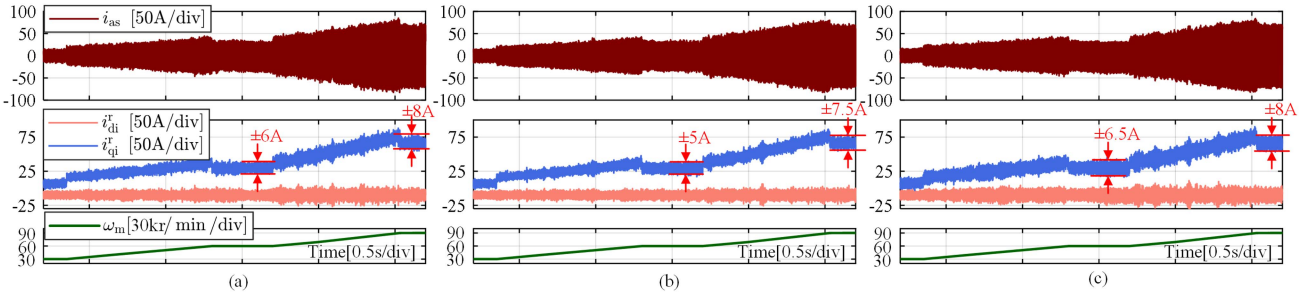

Fig. 14. Comparative experimental results of speed ramps with different AD methods. (a) Proposed APF method. (b) General single-sensor AD method [16]. (c) Improved robust NF method [23].

It is evident that the system maintains stability, which is in alignment with the outcomes observed in Fig. 8.

In summary, the APF-based AD method exhibits a broader stable range, thereby demonstrating enhanced parameter robustness. This attribute is a pivotal factor contributing to the APF's superiority over other filter-based methods.

B. Experimental Comparison With Existing AD Methods

As already mentioned in [18] and earlier analysis of NF in Section IV-B, when the resonant frequency f_p^r is near $f_s/3$, the NF only provides a small PM with low robustness and cannot guarantee the system stability once the resonant frequency f_p^r crosses $f_s/3$. For the system under investigation in this paper, when the operating frequency f_r is 1500 Hz, the resonant frequency of the system, f_p^r (i.e., 13.11 kHz), is less than $f_s/3$ (i.e., 13.33 kHz). Consequently, this test was not conducted and was substituted by the improved robust NF method [23].

A series of comparative experiments were conducted to assess the AD performance of the proposed method in comparison to a general single-sensor AD method [16] and improved robust NF method [23] by increasing the rotational speed from 30 to 60 to 90 kr/min in the speed control mode, as illustrated in Fig. 14, respectively. The motor phase current FFT analysis of three methods at different speed are depicted in Fig. 15. It can be concluded that for inverter-side current feedback control, all three methods exhibit strong resonance suppression capability,

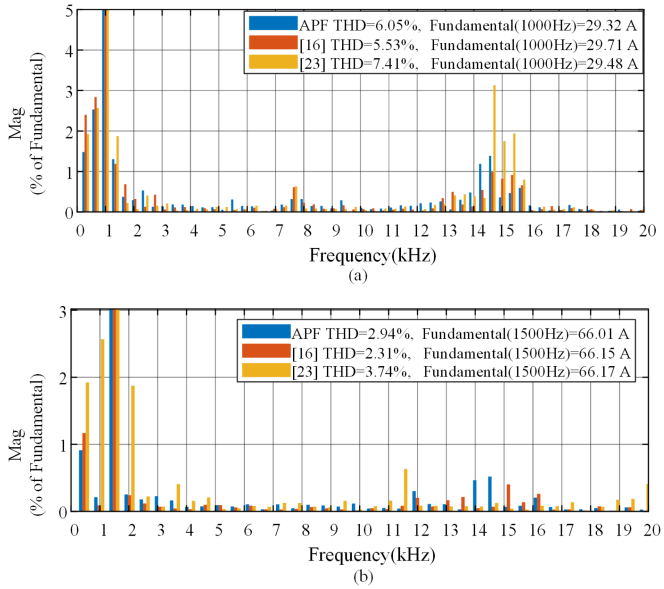

Fig. 15. FFT analysis of phase A current with three different AD methods at different operating frequencies. (a) $f_r = 1000$ Hz. (b) $f_r = 1500$ Hz.

and the proposed APF method has similar motor phase current THD values and steady-state performance as method in [16].

This experimental phenomenon can be theoretically elucidated using the poles diagram of the three methods, as presented

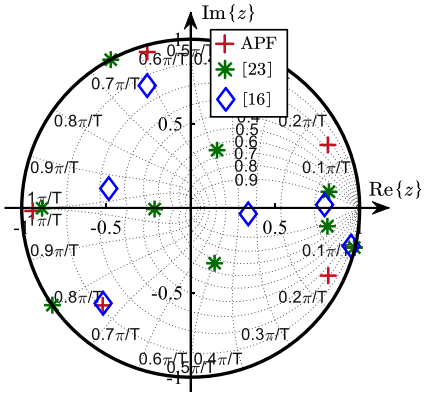

Fig. 16. Poles map of different AD methods.

TABLE III
COMPUTATIONAL TIME OF AD CONTROLLERS

	Proposed Method	[23]	[16]
Computational Time	3.4 μs	4.7μs	11.2μs

in Fig. 16. It can be observed that although the magnitude attenuator was employed in [23], the poles still lie on the edge of the unit circle, their damping is relatively low—resulting in greater current ripple. Since [16] employs the virtual-resistance method to enable arbitrary configuration of the damping ratio, it can be seen that the damping of the system's resonant poles is relatively high, leading to minimal current ripple.

To further emphasize the advantages of the proposed algorithm, a comparison of the computational time of the three methods is presented in Table III. Notably, the proposed method requires fewer computational resources and time than [16] and [23], while achieving a similar AD effect. Consequently, the proposed method is particularly well-suited for systems characterized with higher PWM switching and updating frequency.

C. Experimental Comparison With Different Filter-Based Damping

Previous analysis indicates that since the DF lacks adjustable parameters, experimental verification of its stability requires modifying actual filter parameters. Increasing the filter capacitor from 3.3 to 4 μF decreases the system's resonant frequency from the initial 14.61 to 13.27 kHz. When the operating frequency increases to 1500 Hz, the synchronous resonant frequency drops to 11.02 kHz—below DF's lower stability margin ($3f_s$ /10 = 12 kHz), leading to system instability, as shown in Fig. 17(a). The theoretically calculated instability speed of 76 kr/min closely aligns with the experimentally observed value of 79 kr/min, validating the analytical model.

Fig. 17(b) illustrates the LPF stability validation experiment, where the system becomes unstable at approximately 78 kr/min, exhibiting increased current fluctuations. This result is roughly consistent with the simulation analysis, confirming the LPF's stability boundary prediction.

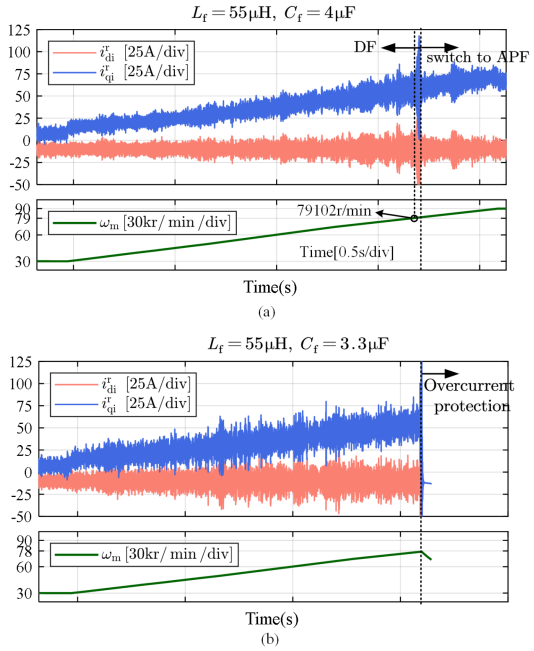

Fig. 17. Experimental results of different filter-based AD methods. (a) DF-based AD. (b) LPF-based AD.

ADF stability regions of the different filters (Fig. 5 in Section IV), multiindex analysis (Fig. 6 in Section IV-C), poles map comparison (Fig. 8 in Section VI-A), simulation results (Fig. 13 in Section VII-A), and experimental data (Fig. 17 in Section VII-C) collectively confirm APF superiority over both the LPF and DF. Therefore, based on the comprehensive analysis and validation presented in this article, for inverter-side current feedback systems employing ADF, the APF is optimal choice over other filter alternatives.

D. Experimental Verification of Parameters Robustness

The parameter mismatch experiments are performed in current control mode. The responses of the motor phase current and dq-axes currents of inverter-side are measured, when a 20 A stepwise change is applied in the q-axis currents $i^{\mathrm{r}}_{\mathrm{qi}}$. Since the load torque of compressor-type motor is proportional to the square of the rotational speed, the motor will gradually accelerate until the developed torque equilibrates with the load [22]. Fig. 18(a) illustrates the current control performance in the context of the proposed control strategy with accurate parameters, and the results of the multiparameter mismatch test are shown in Fig. 18(b) to (d). The following six cases are established to validate the multiparameter robustness of the proposed APF method:

1) Case 1: $4\hat{R}_{\mathrm{s}} = R_{\mathrm{s}}$ and $2\hat{L}_{\mathrm{s}} = L_{\mathrm{s}}$
2) Case 2: $0.5\hat{R}_{\mathrm{s}} = R_{\mathrm{s}}$ and $0.5\hat{L}_{\mathrm{s}} = L_{\mathrm{s}}$
3) Case 3: $1.5\hat{L}_{\mathrm{s}} = L_{\mathrm{s}}$, $1.15\hat{L}_{\mathrm{f}} = L_{\mathrm{f}}$ and $1.15\hat{C}_{\mathrm{f}} = C_{\mathrm{f}}$
4) Case 4: $1.5\hat{L}_{\mathrm{s}} = L_{\mathrm{s}}$, $1.15\hat{L}_{\mathrm{f}} = L_{\mathrm{f}}$ and $0.85\hat{C}_{\mathrm{f}} = C_{\mathrm{f}}$
5) Case 5: $0.7\hat{L}_{\mathrm{s}} = L_{\mathrm{s}}$, $0.85\hat{L}_{\mathrm{f}} = L_{\mathrm{f}}$ and $1.15\hat{C}_{\mathrm{f}} = C_{\mathrm{f}}$
6) Case 6: $0.7\hat{L}_{\mathrm{s}} = L_{\mathrm{s}}$, $0.85\hat{L}_{\mathrm{f}} = L_{\mathrm{f}}$ and $0.85\hat{C}_{\mathrm{f}} = C_{\mathrm{f}}$.

In the parametric robustness analysis, we consider that the motor parameters are unchanged, but we change the controller

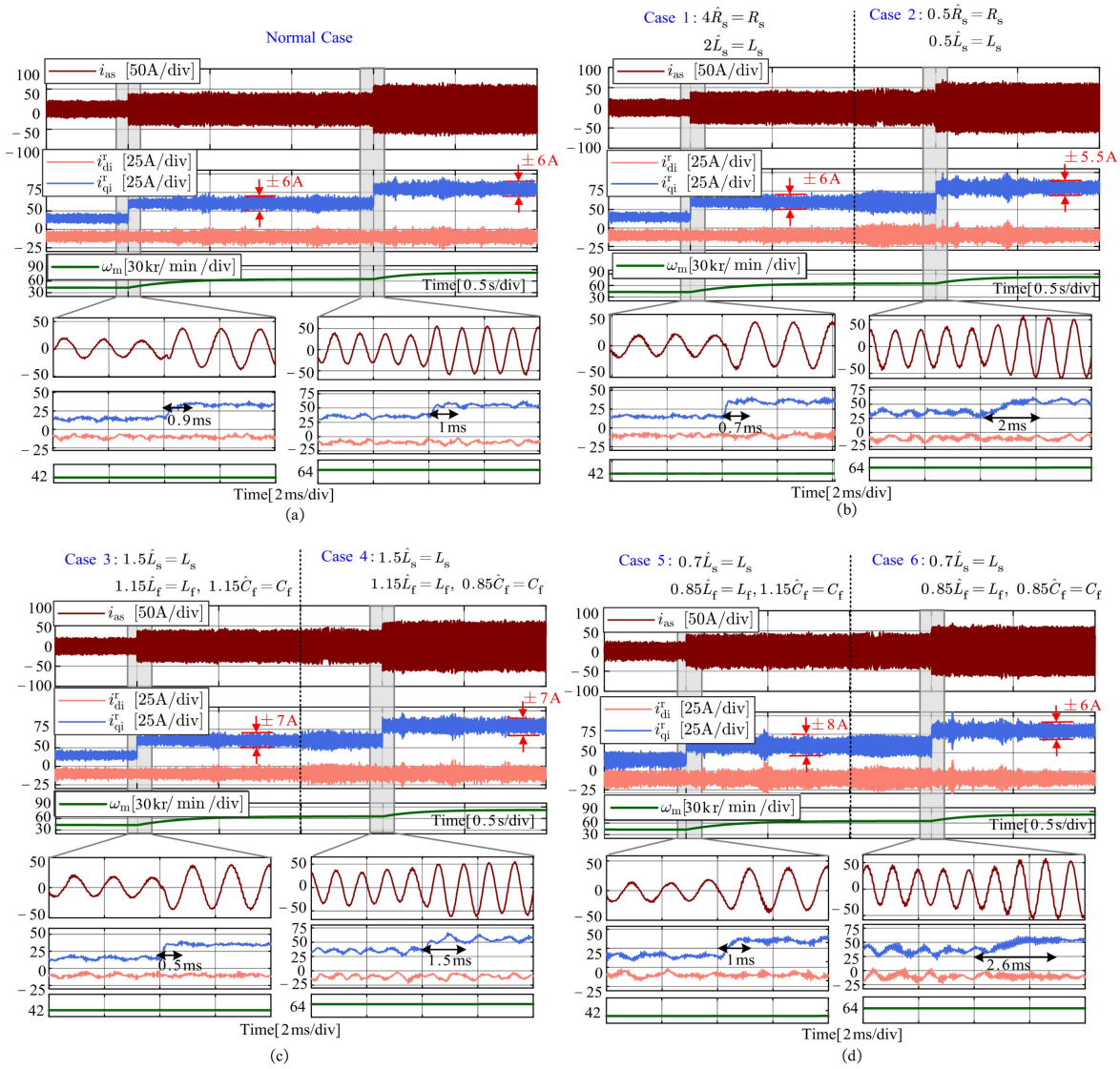

Fig. 18. Robust experimental verification of the proposed APF method. (a) Normal case with accurate parameters. (b) Case 1 and Case 2. (c) Case 3 and Case 4. (d) Case 5 and Case 6.

parameters inversely, e.g., $L_s = 2\hat{L}_s$, then $\hat{L}_s = 0.5L_s$. K and r are calculated offline based on the changed parameters and are made into look-up tables (LUTs) to be stored in the controller. Taking Case 1 as an example, when $\hat{L}_s = 0.5L_s$, at the controller side it is considered that the inductance on the motor side become smaller, leading to an increased resonance frequency due to this parameter change. At this time, the phase delay of the system itself is also considered to be larger at resonance frequency, so under the same PM, the phase delay that should be provided by the APF will be reduced, as outlined in Section V. The aforementioned analysis is anticipated to result in a decrease in r and an increase in K, thereby accelerating the current loop response, as shown in the first enlarged image of Fig. 18(b).

As shown in Fig. 18(b), when the L_s is varied widely, especially when it is reduced, both the dynamic and steady state performance of the system are degraded. For the extreme case Case 6, as shown in Fig. 18(d), the worst steady state and dynamic performance of the system is achieved when both the filter parameters and the inductance parameters are reduced simultaneously. Nevertheless, when the parameters increase, as in Case 1 and Case 3, there is less impact on the performance of the system.

The results of the experiment demonstrate the stability of the proposed method and the analysis in Section VI-A. Obviously, the multiparameter discrepancies result in a degradation of the dynamic and steady state performance of the system, particularly in the case of Case 6. However, this degradation is more limited in scope and remains within acceptable limits.

VIII. Conclusion

This article not only proposes a simple and intuitive graphical method for the comparison and evaluation of various ADFs, but also gives the optimal one, APF, based on multiple performance indicators. Then, a high performance current controller composed of an APF and a dynamic decoupling controller for

LC-HSPMSM is proposed. The selection range of the studied scheme parameters was co-designed to satisfy all stability margins. The simulation results prove the effectiveness of the APF algorithm and its superiority over other ADFs. Furthermore, in comparison with the complex methods reported in recent papers, the proposed APF-based method features a simple structure and is capable of achieving similar performance. This suggests that it is particularly well-suited for systems characterized by higher PWM switching and updating frequencies. The multiparameter mismatch experimental results also show that the proposed method can tolerate $\pm 15\%$ error of filter parameters and (-30%∼+50%) error of motor inductance, simultaneously.

In the aforementioned converter system with an LC filter, most current controllers achieve two-degree-of-freedom functions, with one degree of freedom utilized for reference tracking and the other to achieve resonance suppress. However, the issue of disturbance rejection remains unaddressed—an issue that merits attention in future research. Another point worth studying is to realize parameter identification via signal injection or observer design to achieve adaptive control, thereby further enhancing system robustness and control performance.

Appendix A
Discretization of Different Filters

As posited in this article, the z-domain transfer function $G_{\mathrm{f}}(z)$ can be expressed in generic form as follows for the first- and second-order damping filters under discussion

$$G_{\mathrm{f}}(z) = \frac{a_2 z^2 + a_1 z + a_0}{b_2 z^2 + b_1 z + b_0}. \tag{20}$$

The Tustin method is utilized to discretize LPF, APF and PLF to obtain the transfer function in the z-domain

$$G_{\mathrm{f\_LPF}}(z) = \frac{\omega_{\mathrm{c}} T_{\mathrm{s}} z + \omega_{\mathrm{c}} T_{\mathrm{s}}}{(\omega_{\mathrm{c}} T_{\mathrm{s}} + 2)\, z + (\omega_{\mathrm{c}} T_{\mathrm{s}} - 2)} \tag{21}$$

$$G_{\mathrm{f\_PLF}}(z) = \frac{\omega_{\mathrm{pf}} (\omega_{\mathrm{zf}} T_{\mathrm{s}} + 2)\, z + \omega_{\mathrm{pf}} (\omega_{\mathrm{zf}} T_{\mathrm{s}} - 2)}{\omega_{\mathrm{zf}} (\omega_{\mathrm{pf}} T_{\mathrm{s}} + 2)\, z + \omega_{\mathrm{zf}} (\omega_{\mathrm{pf}} T_{\mathrm{s}} - 2)}. \tag{22}$$

In the context of NF and QNF, since the notch frequency ω_{n} should remain unchanged in z-domain, the Tustin method with prewarping at ω_{n}, is employed, as shown in the Table IV.

Appendix B
Calculation on Cut-Off Frequencies in Low and High Frequency

For the cut-off frequency at low frequency, it can be calculated according to the low frequency part of the open-loop transfer function. With accurate parameters, the transfer function can be expressed as

$$G_{\mathrm{oll}}(z) = \frac{K}{z - 1}. \tag{23}$$

Then, let the magnitude–frequency characteristic of (23) be 1, and the cut-off frequency f_{cp1} at low frequency can be calculated

$$f_{\mathrm{cp1}} = \frac{1}{\pi T_{\mathrm{s}}} \arcsin\left(\frac{K}{2}\right). \tag{24}$$

TABLE IV
Discretization of NF and QNF

Filter	NF	QNF
Discretization method	Tustin with prewarping at ω_{n}	Tustin with prewarping at ω_{n}
a_2	1	$\zeta_{\mathrm{z}} \sin(\omega_{\mathrm{n}} T_{\mathrm{s}}) + 1$
a_1	$-2\cos(\omega_{\mathrm{n}} T_{\mathrm{s}})$	$-2\cos(\omega_{\mathrm{n}} T_{\mathrm{s}})$
a_0	1	$-\zeta_{\mathrm{z}} \sin(\omega_{\mathrm{n}} T_{\mathrm{s}}) + 1$
b_2	$\zeta_{\mathrm{n}} \sin(\omega_{\mathrm{n}} T_{\mathrm{s}}) + 1$	$\zeta_{\mathrm{p}} \sin(\omega_{\mathrm{n}} T_{\mathrm{s}}) + 1$
b_1	$-2\cos(\omega_{\mathrm{n}} T_{\mathrm{s}})$	$-2\cos(\omega_{\mathrm{n}} T_{\mathrm{s}})$
b_0	$-\zeta_{\mathrm{n}} \sin(\omega_{\mathrm{n}} T_{\mathrm{s}}) + 1$	$-\zeta_{\mathrm{p}} \sin(\omega_{\mathrm{n}} T_{\mathrm{s}}) + 1$

For the cut-off frequency at high frequency, it can still be calculated according to the above steps. The magnitude-frequency characteristic of $G_{\mathrm{olh}}(z)$ can be expressed as

$$\underbrace{K \frac{R_{\mathrm{s}} b}{1 - a}}_{\eta} \left| \frac{z e^{\mathrm{j}\omega_{\mathrm{r}} T_{\mathrm{s}}} - a}{z - 1} \right| \left| \frac{z e^{\mathrm{j}\omega_{\mathrm{r}} T_{\mathrm{s}}} - 1}{z^2 e^{2\mathrm{j}\omega_{\mathrm{r}} T_{\mathrm{s}}} - 2z e^{\mathrm{j}\omega_{\mathrm{r}} T_{\mathrm{s}}} \cos(\omega_{\mathrm{p}} T_{\mathrm{s}}) + 1} \right|$$

$$\approx \eta \left| \frac{z e^{\mathrm{j}\omega_{\mathrm{r}} T_{\mathrm{s}}} - 1}{z^2 e^{2\mathrm{j}\omega_{\mathrm{r}} T_{\mathrm{s}}} - 2z e^{\mathrm{j}\omega_{\mathrm{r}} T_{\mathrm{s}}} \cos(\omega_{\mathrm{p}} T_{\mathrm{s}}) + 1} \right|. \tag{25}$$

Then, let the above equation be 1, and the cut-off frequency f_{cp2} at high frequency can be calculated

$$f_{\mathrm{cp2}} = \frac{1}{2\pi T_{\mathrm{s}}} \arccos\left(\frac{-\eta^2 + 4\lambda + \eta\sqrt{\eta^2 - 8\lambda + 8}}{4} \right) - f_{\mathrm{r}} \tag{26}$$

where $\lambda = \cos(\omega_{\mathrm{p}} T_{\mathrm{s}})$.

References

[1] M. M. Qasim, D. M. Otten, J. H. Lang, J. L. Kirtley, and D. J. Perreault, "Comparison of inverter topologies for high-speed motor drive applications," *IEEE Trans. Power Electron.*, vol. 39, no. 6, pp. 7404–7422, Jun. 2024.

[2] C. Zwyssig, S. D. Round, and J. W. Kolar, "An ultrahigh-speed, low power electrical drive system," *IEEE Trans. Ind. Electron.*, vol. 55, no. 2, pp. 577–585, Feb. 2008.

[3] F. Nishanth, M. Johnson, and E. L. Severson, "A review of thermal analysis and management of power dense electric machines," in *Proc. IEEE Int. Electric Mach. Drives Conf.*, 2021, pp. 1–8.

[4] D. A. Rendusara and P. N. Enjeti, "An improved inverter output filter configuration reduces common and differential modes dv/dt at the motor terminals in PWM drive systems," *IEEE Trans. Power Electron.*, vol. 13, no. 6, pp. 1135–1143, Nov. 1998.

[5] N. Vaishnav, N. K. Bajjuri, and A. K. Jain, "Inductor selection, improved active damping, and speed sensorless operation without voltage sensors in IM drive with LC filter," *IEEE Trans. Power Electron.*, vol. 37, no. 12, pp. 15272–15282, Dec. 2022.

[6] M. Antivachis, P. S. Niklaus, D. Bortis, and J. W. Kolar, "Input/output EMI filter design for three-phase ultra-high speed motor drive gan inverter stage," *CPSS Trans. Power Electron Appl.*, vol. 6, no. 1, pp. 74–92, Mar. 2021.

[7] S. G. Parker, B. P. McGrath, and D. G. Holmes, "Regions of active damping control for LCL filters," *IEEE Trans. Ind. Appl.*, vol. 50, no. 1, pp. 424–432, Jan./Feb. 2014.

[8] H.-G. Choi, K. Lee, and J.-I. Ha, "Design and control method for a surface-mounted permanent magnet motor drive system with passive output power network," *IEEE Trans. Power Electron.*, vol. 35, no. 4, pp. 3891–3905, Apr. 2020.

[9] T. Liu, J. Liu, Z. Liu, and Z. Liu, "A study of virtual resistor-based active damping alternatives for LCL resonance in grid-connected voltage source inverters," *IEEE Trans. Power Electron.*, vol. 35, no. 1, pp. 247–262, Jan. 2020.
[10] X. Li, X. Wu, Y. Geng, X. Yuan, C. Xia, and X. Zhang, "Wide damping region for LCL-type grid-connected inverter with an improved capacitorcurrent-feedback method," *IEEE Trans. Power Electron.*, vol. 30, no. 9, pp. 5247–5259, Sep. 2015.
[11] Y. He, X. Wang, X. Ruan, D. Pan, X. Xu, and F. Liu, "Capacitor-current proportional-integral positive feedback active damping for LCL-type grid-connected inverter to achieve high robustness against grid impedance variation," *IEEE Trans. Power Electron.*, vol. 34, no. 12, pp. 12423–12436, Dec. 2019.
[12] H. Zhang, X. Wang, Y. He, D. Pan, and X. Ruan, "A compensation method to eliminate the impact of time delay on capacitor-current active damping," in *IEEE Trans. Ind. Electron.*, vol. 69, no. 7, pp. 7512–7516, Jul. 2022.
[13] X. Wang, F. Blaabjerg, and P. C. Loh, "Virtual RC damping of LCLfiltered voltage source converters with extended selective harmonic compensation," *IEEE Trans. Power Electron.*, vol. 30, no. 9, pp. 4726–4737, Sep. 2015.
[14] L. Zhou et al., "Inverter-current-Feedback resonance-suppression method for LCL-type DG system to reduce resonance-frequency offset and grid-inductance effect," *IEEE Trans. Ind. Electron.*, vol. 65, no. 9, pp. 7036–7048, Sep. 2018.
[15] Z. Lyu and L. Wu, "Current control scheme for LC-Equipped PMSM drive considering decoupling and resonance suppression in synchronous complex-vector frame," *IEEE J. Emerg. Sel. Topics Power Electron.*, vol. 11, no. 2, pp. 2061–2073, Apr. 2023.
[16] Y. Yao, Y. Huang, F. Peng, J. Dong, and Z. Zhu, "A general single-sensor damping framework for LCL-Equipped high-speed PMSM drives," *IEEE Trans. Ind. Electron.*, vol. 70, no. 5, pp. 5375–5380, May 2023.
[17] J. Dannehl, M. Liserre, and F. W. Fuchs, "Filter-based active damping of voltage source converters with LCL filter," *IEEE Trans. Ind. Electron.*, vol. 58, no. 8, pp. 3623–3633, Aug. 2011.
[18] W. Yao, Y. Yang, X. Zhang, F. Blaabjerg, and P. C. Loh, "Design and analysis of robust active damping for LCL filters using digital notch filters," *IEEE Trans. Power Electron.*, vol. 32, no. 3, pp. 2360–2375, Mar. 2017.
[19] Z. Lyu and L. Wu, "Resonant frequency deviation analysis and modified notch filter-based active damping for SiC-based PMSM drive with sine wave filter," *IEEE Trans. Energy Convers*, vol. 38, no. 1, pp. 417–427, Mar. 2023.
[20] M. Yang et al., "Resonance suppression and EMI reduction of GaN-Based motor drive with sine wave filter," *IEEE Trans. Ind. Appl.*, vol. 56, no. 3, pp. 2741–2751, May/Jun. 2020.
[21] W. Yao, Y. Yang, Y. Xu, F. Blaabjerg, S. Liu, and G. Wilson, "Phase reshaping via all-pass filters for robust LCL-Filter active damping," *IEEE Trans. Power Electron.*, vol. 35, no. 3, pp. 3114–3126, Mar. 2020.
[22] L. Shi, C. Cheng, M. Hu, W. Hua, and C. Lu, "A robust two-degree-of-freedom current control strategy for LCL-equipped high-speed PMSMs," *IEEE Trans. Power Electron.*, vol. 39, no. 12, pp. 15954–15966, Dec. 2024.
[23] Y. Yao, D. Xu, Y. Chen, F. Peng, and Y. Huang, "Robust notch filter-based active damping design for LCL-equipped high-speed PMSMs considering dual resonance problem," *IEEE Trans. Ind. Electron.*, vol. 71, no. 11, pp. 13845–13854, Nov. 2024.
[24] J. Kukkola, M. Hinkkanen, and K. Zenger, "Observer-based state-space current controller for a grid converter equipped with an LCL filter: Analytical method for direct discrete-time design," *IEEE Trans. Ind. Appl.*, vol. 51, no. 5, pp. 4079–4090, Sep./Oct. 2015.
[25] C. A. Busada, S. G. Jorge, and J. A. Solsona, "Full-state feedback equivalent controller for active damping in LCL-filtered grid-connected inverters using a reduced number of sensors," *IEEE Trans. Ind. Electron.*, vol. 62, no. 10, pp. 5993–6002, Oct. 2015.
[26] J. Dannehl, F. W. Fuchs, and P. B. Thøgersen, "PI state space current control of grid-connected PWM converters with LCL filters," *IEEE Trans. Power Electron.*, vol. 25, no. 9, pp. 2320–2330, Sep. 2010.
[27] H. Kim, M. W. Degner, J. M. Guerrero, F. Briz, and R. D. Lorenz, "Discrete-time current regulator design for AC machine drives," *IEEE Trans. Ind. Appl.*, vol. 46, no. 4, pp. 1425–1435, Jul./Aug. 2010.

Ling Meng was born in Shandong, China. He received the B.S. degree in automotive engineering from the College of Automotive Engineering, Jilin University, Changchun, China, in 2021. He is currently working toward the Ph.D. degree in automotive engineering with the School of Automotive Studies, Tongji University, Shanghai, China.

His research interests include high-performance ac drive systems, sensorless control algorithm of high-speed PMSMs and drive system equipped with *LCL* filters.

Yuan Zhu was born in Jiangsu, China, in 1976. He received the double B.S. degrees in automotive engineering and computer application technology, as well as the Ph.D. degree in automotive engineering from all from Tsinghua University, Beijing, China, in 1998 and 2003, respectively.

He served as an Assistant Research Scientist with the Department of Automotive Engineering, Tsinghua University from 2003 to 2005. Since 2005, he has been working as an Associate Professor with the Sino-German School and the School of Automotive Studies, Tongji University. From 2014 to 2019, he held the Hans L. Merkle Foundation-Bosch Endowed Chair for Automotive Systems at Tongji University. Since 2023, he has been the Director of the School of Automotive Studies, Tongji University-Vector Automotive Technology Joint Laboratory. Since 2024, he has held the Infineon Endowed Chair for Microcontroller and Embedded Systems at Tongji University. His current research interests include control and parameter identification for electric drive systems and high-speed PMSMs, as well as embedded software systems.

Yunpeng Zhou was born in Shandong, China. He received the B.S. degree in automotive engineering from the College of Automotive Engineering, Jilin University, Changchun, China, in 2023. He is currently working toward the M.S. degree in automotive engineering with the School of Automotive Studies, Tongji University, Shanghai, China.

His research direction is the control technology of high-speed permanent magnet synchronous motors with LC filters.